# Supporting Information

# High Performance 1D-2D CuO/$MoS_2$ Photodetector Enabled by Femtosecond Laser-induced Contact Engineering

*Jinpeng Huo[1], Guisheng Zou[1], Yu Xiao[1], Tianming Sun[1,2],Bin Feng[1], Daozhi Shen[3], Luchan Lin[4], Wengan Wang[1], Zhanwen A[1], , Lei Liu[1,*]*

[1] Department of Mechanical Engineering, State Key Laboratory of Tribology, Key Laboratory for Advanced Manufacturing by Materials Processing Technology, Ministry of Education of PR China, Tsinghua University, Beijing 100084, P. R. China

[2] Taiyuan University of Technology, Taiyuan 030024, China

[3] School of Mechanical Engineering, Shanghai Jiao Tong University, Shanghai, 200240 China

[4] Shanghai Key Laboratory of Materials Laser Processing and Modification School of Materials Science and Engineering, Shanghai Jiao Tong University, Shanghai 200240, China

* Corresponding author. E-mail address: liulei@tsinghua.edu.cn

## Note 1. Experiment section

**Device Fabrication:** Detailed device fabrication process is illustrated in Figure S1. Cr/Au (5 nm and 25 nm respectively) electrodes with 2 μm finger spacing on the chip were fabricated by optical lithography and lift-off process on oxidized Si substrate (300 nm $SiO_2$). The electrodes were rinsed with high purity acetone (99.99%) and ethanol (≥99.5%) for 10min before the h-BN/$MoS_2$/CuO heterostructure was assembled. After cleaning process, dry transfer method was carried out to place CuO NWs, $MoS_2$ flakes and h-BN flakes onto specified position. CuO NWs were synthesized by the thermal oxidation of Cu mesh at 450 °C for 4 h at atmosphere in muffle furnace[1], then they were dispersed in an ethanol solution following by an ultrasonic bath for 60 s to fabricate the NWs suspensions. After that, the CuO NWs solution were continuously drop-cast on the polydimethylsiloxane (PDMS) film and naturally air-dried. During dry transfer process, the thermal-released PDMS tape was precisely attached to the chip using a three-axis manipulator and an optical microscope. Then the sample was heated at approximately 80 °C for 10 min to release CuO NWs onto the substrate. Multilayer $MoS_2$ and h-BN was mechanically exfoliated from bulk $MoS_2$ and h-BN using an adhesive tape, then thermal-released PDMS tape was used to transfer the $MoS_2$ and h-BN flakes onto the substrate orderly. The sample was heated at approximately 80 °C for 20 min to release 2D materials onto the substrate to form the h-BN/$MoS_2$/CuO heterostructure.

**BN-Encapsulated Femtosecond Laser Treatment:** Detailed fs laser treatment process is illustrated in Figure S2. Fs laser pluses (800 nm, 1kHz) was generated by a Ti: sapphire mode-locked oscillator with a typical duration of 50 fs. The laser beam passes through an electronic shutter to control the irradiation time, reflective neutral density filters to reduce the laser power density and a polarizer coupling with half wave plate to control the laser polarization direction and laser fluence continuously. An objective lens with numerical aperture (NA=0.4) and long working distance (13 mm) focused the laser beam to a circle area with 10 μm radius at normal incidence. The CCD camera coupling with three-axis electric moving stage system was used to highly

control the spatial location of laser irradiation area. The *in situ* electrical characteristics and photo response of the three-terminal devices were carried out by precise source-meters (Keithley 2636B and Agilent B1500A).

**Analytical Characterization:** Analytical measurements were carried out by X-ray diffraction (XRD, Bruker D8), X-ray photoelectron spectroscopy (XPS, Quantera II), Scanning Electronic Microscopy (SEM, JEOL-7001F-77), Transmission Electron Microscope (TEM, JEOL-2100F), Raman spectroscopy (JY HR-800), and atomic force microscopy (AFM, Bruker Dimension ICON).

## Note 2. The wrapping of $MoS_2$ nanosheet around the CuO NW by ultrafast laser pressure

The wrapping of $MoS_2$ nanosheet around the CuO NW was partly attributed to the pressure during the dry transfer and the gravity of $MoS_2$ and h-BN flakes. However, fs laser irradiation will still cause the more conformal wrapping behavior of $MoS_2$ nanosheet after dry transfer process. Consequently, we believe that the wrapping of $MoS_2$ nanosheet may be attributed to the radiation pressure on the $MoS_2$ flakes. During fs laser irradiation, photons carry momentum thus will push on any object on the path of light by the change in photon momentum[2-4]. When the incident laser is a plane wave, the axial radiation force F for a particle located on the beam axis is proportional to the optical power P:

$$F = \frac{\mathrm{P}\left[2\mathrm{R} + (1-\mathrm{R})\alpha\right]\cos(\theta)}{\mathrm{c}} \qquad \backslash\text{* MERGEFORMAT (1)}$$

Where R is the reflectivity of material, α is the fraction of non-reflected light absorbed by the material, θ is the angle of incidence, and c is the speed of light. Equation (1) describes that the absorbed photon will imparts all its momentum and a reflected photon will impart twice its momentum. The reflectivity of $MoS_2$ flakes was estimated to be 0.05 at 800nm and the (1-R)α was higher than 0.4.[5, 6] The irradiation pressure can be calculated by

$$P = \frac{\mathrm{F}}{\mathrm{S}_l} = -\frac{\mathrm{I}\left[2\mathrm{R} + (1-\mathrm{R})\alpha\right]\cos(\theta)}{\mathrm{c}} \quad \text{* MERGEFORMAT (2)}$$

$$I = \frac{\mathrm{E}}{\mathrm{t} \times \mathrm{S}_l} \quad \text{* MERGEFORMAT (3)}$$

Where I is the laser power density, E is the pulse energy, t is the duration of fs laser pulse (50 fs), $S_l$ is the laser spot area. The peak power density of fs laser was calculated to be higher than $8\times10^{16}$ W/m$^2$, and the irradiation pressure was estimated to be 0.13 GPa. It was much higher than the pressure during transfer process and the pressure caused by gravity, which is a considerable magnitude on the micro/nano scale. Moreover, if there exists any ablation mass such as organics during fs laser irradiation, the maximum ultrafast pressure of the shock wave will be higher[7], thus significantly improve the interface quality and contact area of 1D-2D mix-dimensioned heterostructure. In conclusion, the thermal effect and pressure effect will cause a higher conformal wrapping around the cylindrical nanowire and form an area contact with CuO NW.

## Note 3. The calculation of responsivity of fs laser treated h-BN/$MoS_2$/CuO heterostructure at forward bias.

The $R_\lambda$ of a photodetector were calculated by using the following equations:

$$R_\lambda = \frac{I_{light} - I_{dark}}{S_{mat} P_{in}} \quad \text{* MERGEFORMAT (4)}$$

where $I_{light} - I_{dark}$ is the photocurrent (A), $S_{mat}$ is the effective area under illumination and $P_{in}$ is the incident light power density. The current at forward bias under an illumination power of 1.8 μW (@525nm) shown in Figure S9 is ~3.56 nA and the dark current is ~1.21 nA. The photocurrent at forward bias was calculated to be

$$I_{ph} = I_{light} - I_{dark} \approx 2.35nA \quad \text{* MERGEFORMAT (5)}$$

The effective area under illumination of h-BN/$MoS_2$/CuO device is defined as the

junction area between CuO NW and $MoS_2$ nanosheet, which can be obtained by multiplying the cross-sectional contact line length ($l_{cross}$) and the length of junction between CuO NW and $MoS_2$ nanosheet ($l_{junction}$) shown in Figure R2b. The SEM images shows that the contact arc between $MoS_2$ and CuO NW was less than 60°, and the radius of the CuO nanowires was ~50 nm, and the length of junction between CuO NW and $MoS_2$ nanosheet was ~5 μm. In this condition the $S_{mat}$ can be calculated to be

$$S_{mat} = r_{CuO}\theta_{arc}l_{junction} \approx 0.05 \times \frac{\pi}{3} \times 5\mu m^2 = 0.262\mu m^2 \text{ * MERGEFORMAT (6)}$$

The illumination fluence was 1.8 μW and the radius of the light spot was ~ 0.4 mm. Thus, the incident light power density can be estimated as

$$P_{in} = \frac{P_{light}}{\pi r^2} = \frac{1.8\mu W}{\pi \times 400\mu m \times 400\mu m} \approx 3.58 \times 10^{-3}\, nW/\mu m^2 \text{ * MERGEFORMAT (7)}$$

The photoresponsivity at forward bias can be calculated by Equation (1.1)

$$R_{525nm} = \frac{I_{light} - I_{dark}}{S_{mat}P_{in}} = \frac{2.35 \times 10^{-9} A}{0.262 \times 3.58 \times 10^{-12} W};\ 2500\, A/W \text{ * MERGEFORMAT (8)}$$

The high calculated photoresponsivity mainly comes from the definition of effective area under illumination of h-BN/$MoS_2$/CuO device. If the $S_{mat}$ is defined as the whole area of device, the photoresponsivity at forward bias will be calculated as

$$R_{525nm} = \frac{I_{light} - I_{dark}}{S_{mat}P_{in}} = \frac{2.35 \times 10^{-9} A}{1600 \times 3.58 \times 10^{-12} W};\ 0.41\, A/W \text{ * MERGEFORMAT (9)}$$

## Note 4. The calculation of EQE of fs laser treated h-BN/$MoS_2$/CuO

**heterostructure at zero bias.**

External quantum efficiency (EQE) represents how many charge carriers are created by one incident photon. In general, EQE is defined as the Equation

$$\mathrm{EQE}=\frac{\mathrm{hc}}{\mathrm{e}\lambda}R_{\lambda} \qquad \backslash^{*}\ \mathrm{MERGEFORMAT}\ (10)$$

Where λ is the exciting wavelength, h is the Planck's constant, c is the velocity of light, and e is the electronic charge. We test the photo response of our device under illumination with wavelength of 525nm at zero bias voltage, where the $MoS_2$/CuO heterojunction is operated in self-powered mode. Figure S10 shows the photo response of h-BN/$MoS_2$/CuO heterostructure under power densities of 2mW/mm$^2$, the responsivity and EQE can be calculated as

$$\mathrm{R}_{525nm}=\frac{\mathrm{I}_{\mathrm{light}}\text{-}\mathrm{I}_{\mathrm{dark}}}{\mathrm{S}_{\mathrm{mat}}\mathrm{P}_{\mathrm{in}}}=\frac{0.09\times10^{-9}\,A}{0.25\times8\times10^{-9}\,W};\ 0.18\,A/W \backslash^{*}$$

MERGEFORMAT (11)

$$\mathrm{EQE}=\frac{\mathrm{hc}}{\mathrm{e}\lambda}R_{\lambda}=\frac{6.626\times10^{-34}\,J\mathrm{gs}\times3\times10^{8}\,m/s}{1.602\times10^{-19}\,C\times5.25\times10^{-7}\,m}\times0.18\,A/W=42\% \backslash^{*}$$

MERGEFORMAT (12)

It can be found in Equation 1.12 that the responsivity and EQE values at zero bias reach 0.18 A/W and 42%, respectively, which not exceed 100% quantum efficiency. This is because that there is no gain mechanism when operating in self-powered mode.

However, when the device at forward bias, the whole heterostructure is work as a phototransistor under illumination, whose mechanism is mostly the photoconductive effect attributed to the trapping of carriers in band tail states in the $MoS_2$ flakes by Hornbeck−Haynes model[8]. Photovoltaic devices depend solely on exciton separation;

the mechanism of Schottky barrier modulation is often different: the photogenerated carriers migrate to the metal interface and are trapped, lowering the Schottky barrier. This, in turn, causes an increase in thermionic emission through the device, leading to high EQE.[9] Moreover, Junseok Seo et al. reported a ultrasensitive photodetection of $MoS_2$ avalanche phototransistors. When the devices were characterized under illumination, the initiation of the breakdown by photogenerated carriers in the channel will manifests itself to excellent photoresponsivity, detectivity and EQE of $\approx 3.4\times10^7$ A $W^{-1}$, $\approx 4.3 \times 10^{16}$ Jones, and $\approx 8.1 \times 10^9$ %, respectively.[10] The high responsivity can be as high as 2500 A/W and the EQE can be up to $6.5\times 10^7$ % for our device, whose gain mechanism might be photoconductive effect avalanche breakdown and carrier injection.

When the device at reverse bias, R and EQE of the device will also increase with the improvement in the source−drain bias, which might be due to the higher carrier concentration under a higher reverse bias. The whole heterostructure is work as a photodiode under illumination, while the photoconductive effect and Schottky barrier modulation still exist in CuO and $MoS_2$.

## Note 5. The calculation of detectivity of h-BN/$MoS_2$/CuO heterostructure at zero bias and reverse bias.

The detectivity of photodetector reflects the ability to detect weak signals from the noise environment. D* can be estimated by the equation which depends on the geometry and noise current:[11, 12]

$$D^{*}=(S_{mat})^{1/2}\frac{R_{\lambda}}{PSD_{overall}} \qquad \backslash* \text{ MERGEFORMAT (13)}$$

For a photodetector which is limited by different sources of noise, the noise current

density (PSD) can be determined from the root mean square of the dark current fluctuations as

$$\mathrm{PSD}_{overall} = \sqrt{\mathrm{PSD}_{\mathrm{shot}}^2 + \mathrm{PSD}_{\mathrm{thermal}}^2 + \mathrm{PSD}_{1/f}^2} \quad \text{(14)}$$

Where $\mathrm{PSD}_{\mathrm{shot}}$, $\mathrm{PSD}_{\mathrm{thermal}}$ and $\mathrm{PSD}_{1/f}$ is the equivalent current spectral density of shot, thermal and 1/f noise, respectively. The equivalent noise current spectral density (PSD) of shot noise can be calculated with the following expression:

$$\mathrm{PSD}_{\mathrm{shot}} = \sqrt{\frac{2qI_d}{\Delta f}} A\ Hz^{1/2} \quad \text{(15)}$$

where $I_d$ is the drain current in the dark at maximum responsivity, $\Delta f$ =1 Hz is the bandwidth and q is the electron charge. Similarly, thermal noise can be calculated as:

$$\mathrm{PSD}_{\mathrm{thermal}} = \sqrt{\frac{4k_B T}{R_{ch}\Delta f}} A\ Hz^{1/2} \quad \text{(16)}$$

where $k_B$ is Boltzmann constant ($1.381\times10^{-23}$ J/K), $R_{Ch}$ is the channel resistance ($=V_d/I_d$), and T = 300 K. There are the third types of noise, 1/f noise, which dominates at low frequencies (<100 kHz). The $\mathrm{PSD}_{\mathrm{thermal}}$ of our device is calculated to be ~$8.1\times10^{-16}$ A $Hz^{1/2}$. When the device is operated at zero bias, the $\mathrm{PSD}_{shot}$ is very low, and the $\mathrm{PSD}_{\mathrm{thermal}}$ is the is the dominant source of the noise current. In this condition, the responsivity is calculated to be ~0.18 A/W, which is shown in Figure S10 and discussed in detail in *Supplement Note 4*. The detectivity calculated at zero bias is about $1.13\times10^{11}$ Jones.

At reverse bias @5V, $\mathrm{PSD}_{\mathrm{shot}}$ becomes high and contributes significantly to the noise current, where $\mathrm{PSD}_{\mathrm{thermal}}$ is lower than $\mathrm{PSD}_{shot} \approx 1.8\times10^{-15}\ A\ Hz^{1/2}$. In this

condition, the responsivity can be as high as 258 A/W at the illumination wavelength of 490 nm, which leading to a higher detectivity:

$$D^{*}=(\frac{S_{mat}}{PSD_{shot}^{2}+PSD_{thermal}^{2}})^{1/2}R_{\lambda}\ ;\ 6.5\times10^{11}\,Jones * MERGEFORMAT (17)$$

If the detectivity is calculated the by assuming that the shot noise from dark current is the dominant source of the noise current, $i_{total} \approx i_{n,s} = \sqrt{2qI_d\Delta f}$ , thus the detectivity can be written as:

$$D^{*}=\frac{R_{\lambda}}{(2qI_d/S_{mat})^{1/2}} \qquad * MERGEFORMAT (18)$$

The calculated detectivity of the heterostructure is as high as $1.07 \times 10^{12}$ Jones.

## Note 6. The photoswitching behavior of h-BN/$MoS_2$/CuO heterostructure compared with $MoS_2$ phototransistor.

Figure 5g the photoswitching behavior for the heterojunction at reverse bias. It can be observed that the current is increased with the measurement time in the first 20 cycles, then it comes to a relatively stable value after 3 min. We speculate that the increasing of photocurrent with time is related to persistent photoconductivity (PPC) effect and photogating (PG) effect of $MoS_2$ flakes[13-15]. The persistent photoconductivity is defined as the light-induced enhancement in conductivity that persists for a long period after termination of photoexcitation, where current does not recover back to its original value even after a prolonged time period. The PPC effect has been attributed to the capture of photogenerated holes in deep intergap states of $MoS_2$. Actually, a major drawback of $MoS_2$ and related hybrid structures for applications in

optoelectronics is its PPC effect, i.e., the device cannot be totally switched off in the dark. Suppressing the PPC effect is therefore of utmost importance to leverage the fundamental features of $MoS_2$ for various technological applications.

In order to characterize persistent photoconductivity effect and photogating effect of $MoS_2$ flakes, we test the dynamic photoresponse of source–drain current of $MoS_2$ FETs in a dark–light–dark cycle, which was shown in Figure S18. It can be observed that the current shows an abrupt increase as soon as the light is turned on which is the result photoexcitation effect. Then it is followed by a much slower current increase, a behavior that can be understood considering that photogenerated holes get trapped and attract more electrons, which gradually increase the channel conductivity by PG effect. Switching off the light results in a very slow decay of the current, where trapped charges cause long sustained conductivity by PPC effect.

In our h-BN/$MoS_2$/CuO heterostructure, the PG and PPC effect also existed in the $MoS_2$ flakes, which will inevitably bring a slight increase of current with the measurement time caused by the increase of channel conductivity. However, the built-in field formed by the band alignment of CuO and $MoS_2$ can significantly suppress the dark current. The photoswitching behavior for the heterojunction at reverse bias shown in Figure 5g exhibits a minimal enhancement of dark current and photocurrent with measure time compared with $MoS_2$ photodetector, which represents possibility to monitor distinguishable current signal changes by light inputs with higher frequency. At last, we propose a possible route to further increases stability by pre-operating the device until it maintains a relatively stable photocurrent value. As shown in Figure 3g,

the device was firstly operating under illumination for 300s, and the subsequent photoresponse results shows that the current was highly stable with measurement time after pre-operating.

## Supplementary Figures

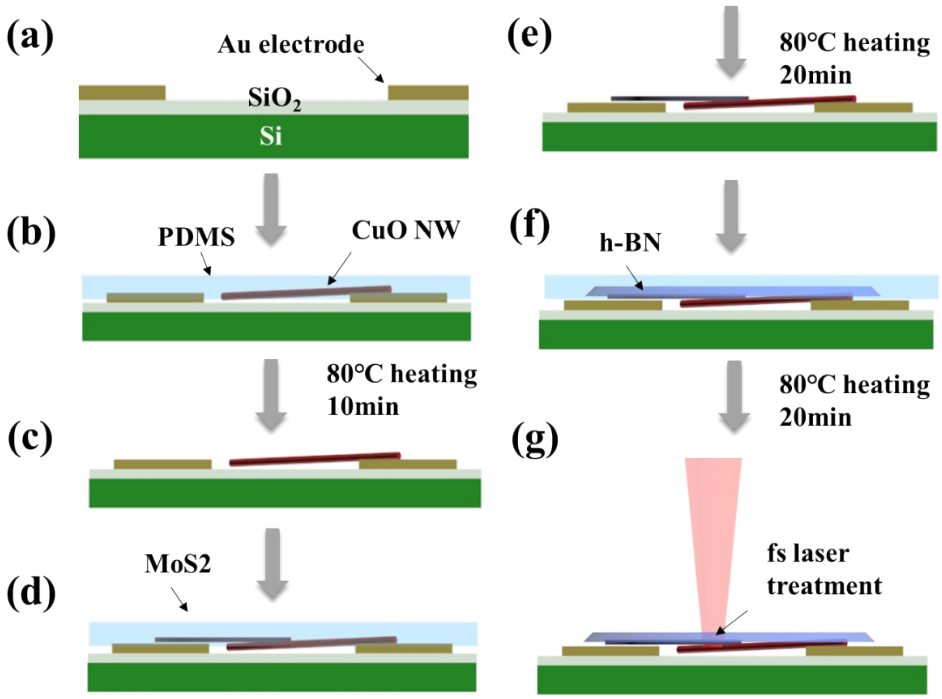


**Figure S1.** The schematic illustration of the device fabrication. (a) The silicon substrate was oxidized and Au electrodes were fabricated by photoetching process. (b)(c) CuO NW synthesized by thermal oxidation was transferred on one side of Au electrode by PDMS. (d)(e) $MoS_2$ nanoflake was mechanically exfoliated and dry transferred onto the substrate. (f) h-BN nanoflake was mechanically exfoliated and dry transferred onto the substrate. (g) Fs laser irradiation treatment was demonstrated after h-BN encapsulation.

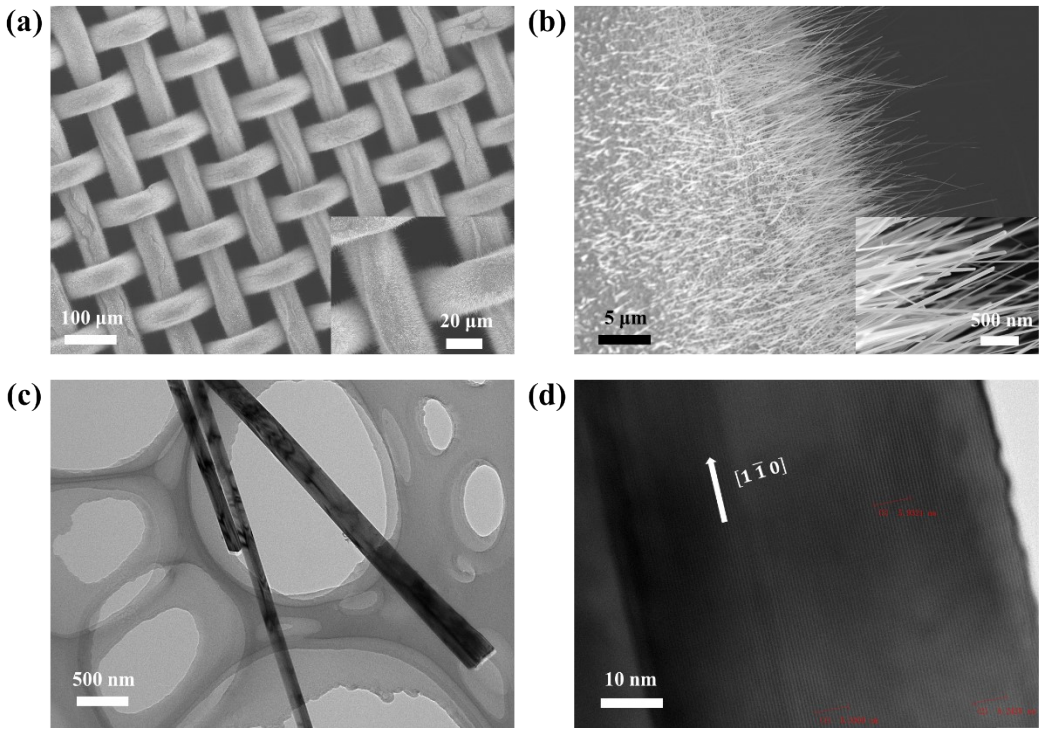


**Figure S2.** SEM and TEM images of CuO NWs synthesized by heating copper grids at 450 °C for 4 h at atmosphere in muffle furnace. (a, b) Typical SEM image of the CuO NWs at different magnifications, indicating the diameter and length of 50 ~ 200 nm and 5 ~ 50 μm, respectively. (c, d) TEM image of as synthesized CuO NWs, indicating a preferential growth orientation along $[1\ \bar{1}\ 0]$ direction.

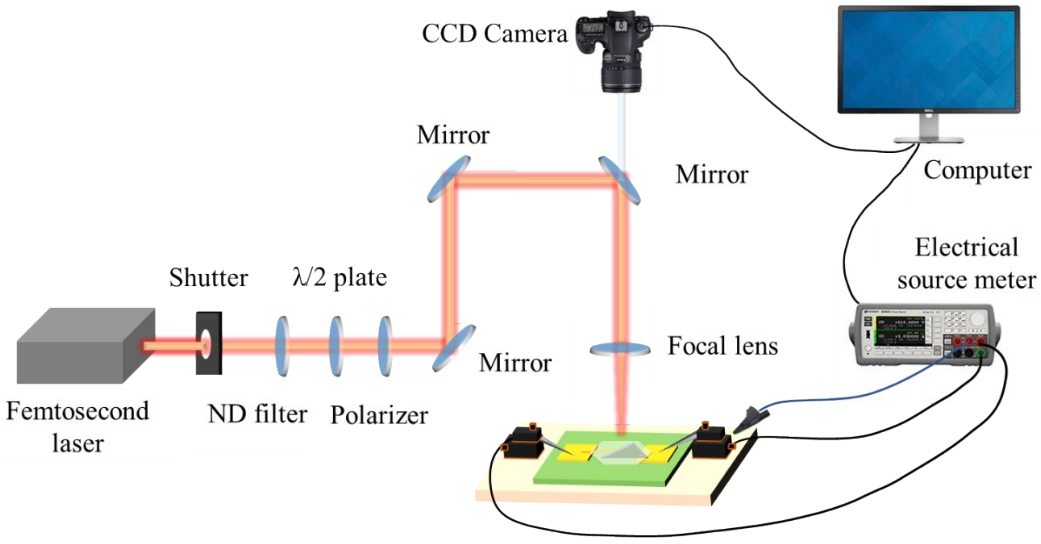


**Figure S3.** The schematic diagram of the BN-encapsulated femtosecond laser treatment and *in situ* electrical characteristics of h-BN/$MoS_2$/CuO heterostructure.

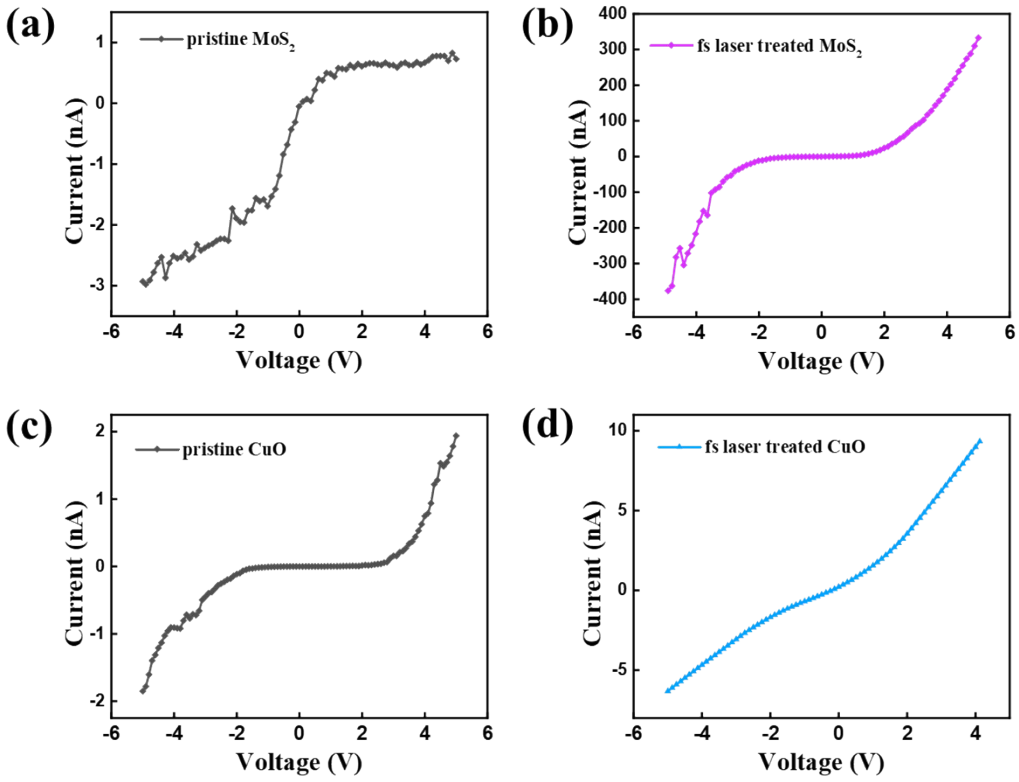


**Figure S4.** Electrical characterization of $MoS_2$ and CuO before and after fs laser irradiation. (a) I-V curve of the pristine Au-$MoS_2$-Au structure. (b) I-V curve of the fs laser treated Au-$MoS_2$-Au structure, indicating a Schottky contact between Au and $MoS_2$. (c) I-V curve of the pristine Au-CuO-Au structure. (d) I-V curve of the fs laser treated Au-CuO-Au structure, indicating a Quasi-Ohmic contact between Au and CuO.

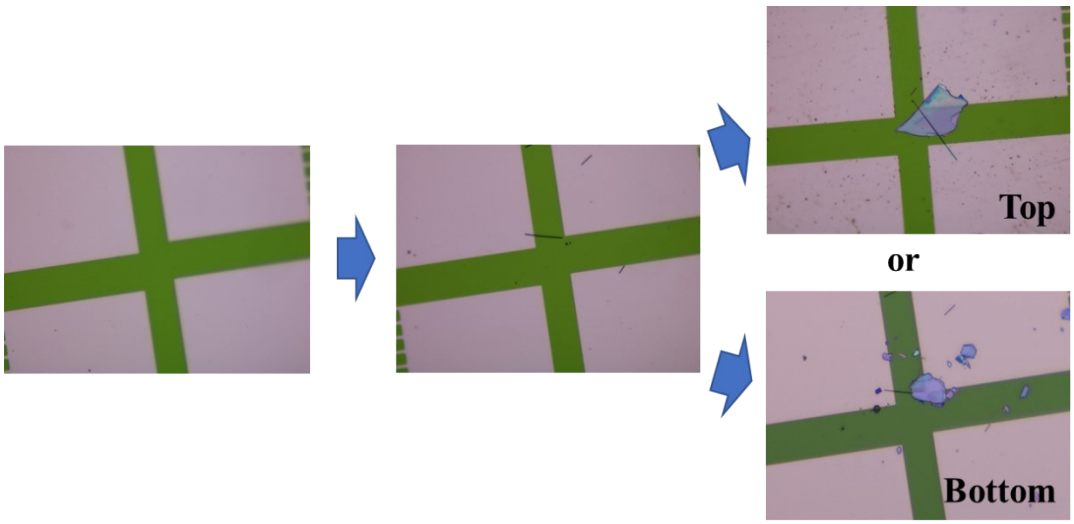


**Figure S5.** Optical imaged of approach for different configuration of CuO-$MoS_2$ 1D-2D p-n

junction. Top: CuO nanowire on MoS2 nanosheet. Down: $MoS_2$ nanosheet on CuO nanowire.

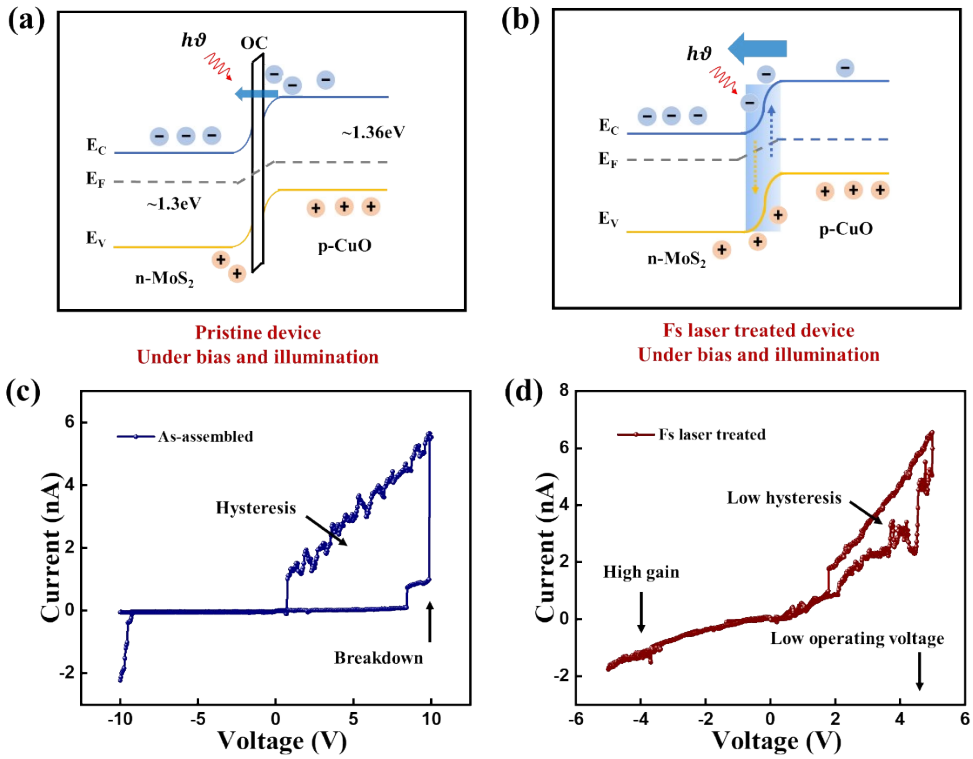


**Figure S6.** Fs laser gain mechanism of photoresponsivity and corresponding electrical characterization. Band diagrams of (a) the pristine and (b) fs laser treated $MoS_2$/CuO NW heterojunction under reverse bias and illumination. Electrical characterization of (c) pristine and (d) fs laser treated $MoS_2$/CuO NW heterojunction under illumination condition.

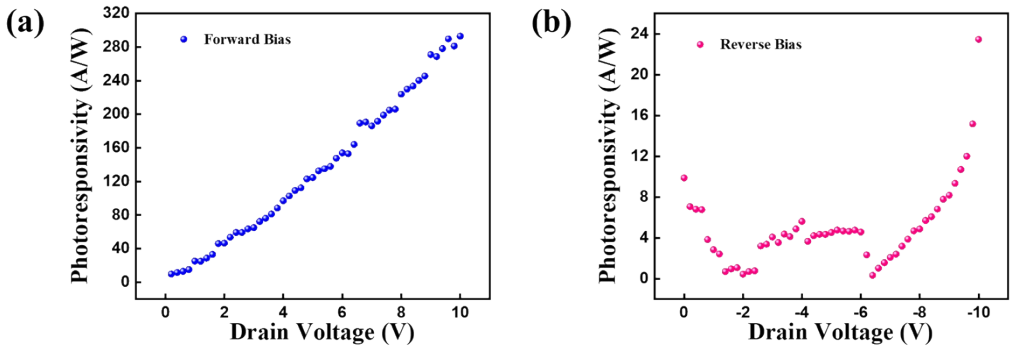


**Figure S7.** Photoresponsivity of the junction at (a) forward and (b) reverse bias under optical irradiation with various source-drain voltage.

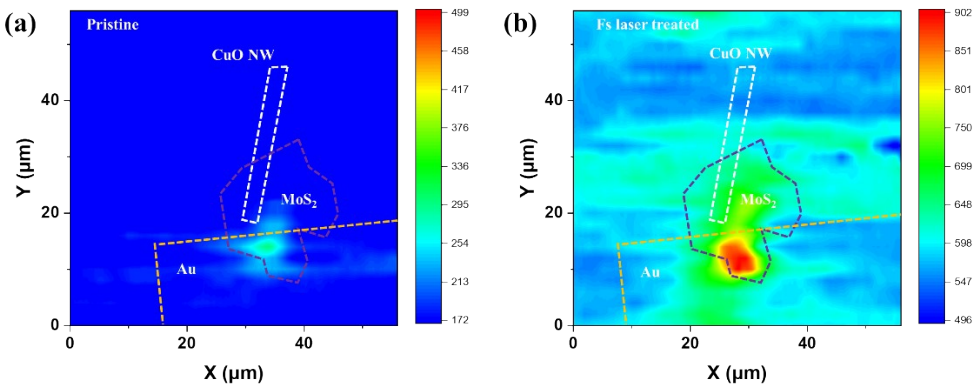


**Figure S8.** Photoinduced response of pristine and fs laser treated h-BN/CuO/$MoS_2$ 1D-2D heterojunction at forward bias. (a) Scanning photocurrent micrograph of as-assembled heterojunction acquired at $V_{DS}$ = 5 V, showing that the photocurrent was mainly generated at the Au-$MoS_2$ interface region. (b) Photocurrent mapping of fs laser treated heterojunction, which shows an increase in photocurrent at the whole $MoS_2$ surface under positive bias. CuO NW, $MoS_2$ and Au electrode are indicated by white, brown and yellow dashed lines, respectively.

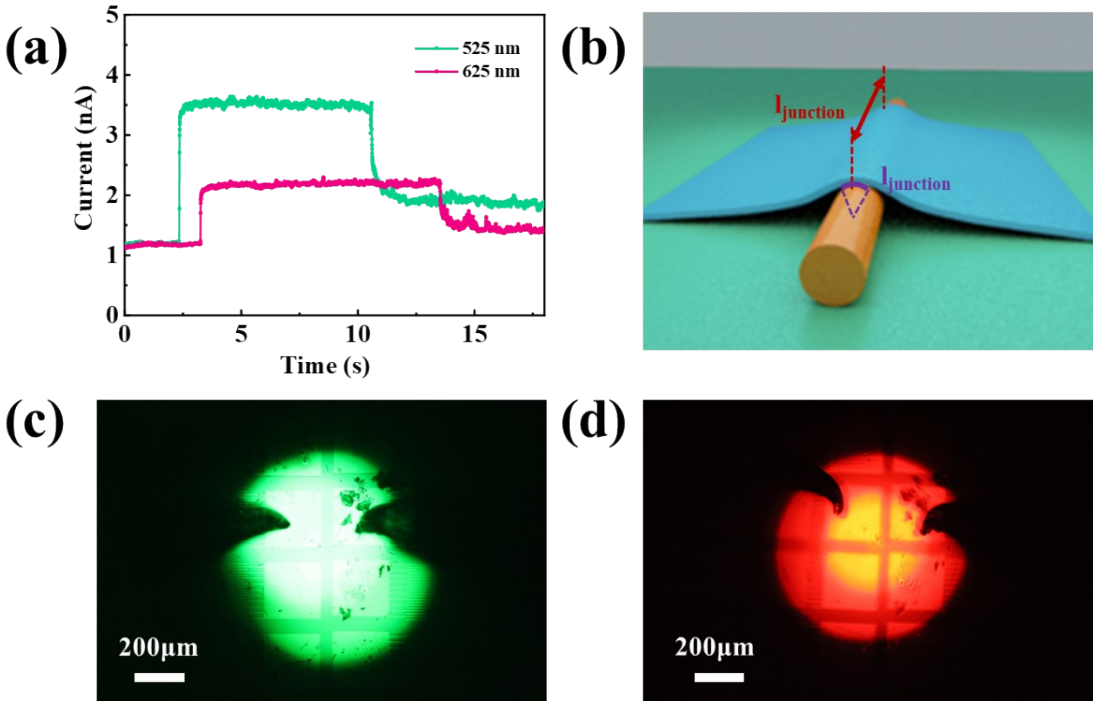

**Figure S9.** (a) Time-resolved photoresponse of the heterojunction at forward bias after fs laser irradiation, recorded under illumination wavelength of 525nm and 625nm. (b) The light absorption area of $MoS_2$/CuO nanosheet-on-1D heterojunction photodetectors which can be obtained by multiplying the cross-sectional contact line length ($l_{cross}$) and the length of junction between CuO NW and $MoS_2$ nanosheet ($l_{junction}$). (c) and (d) Optical images of the incident light with wavelength of 525nm and 625nm.

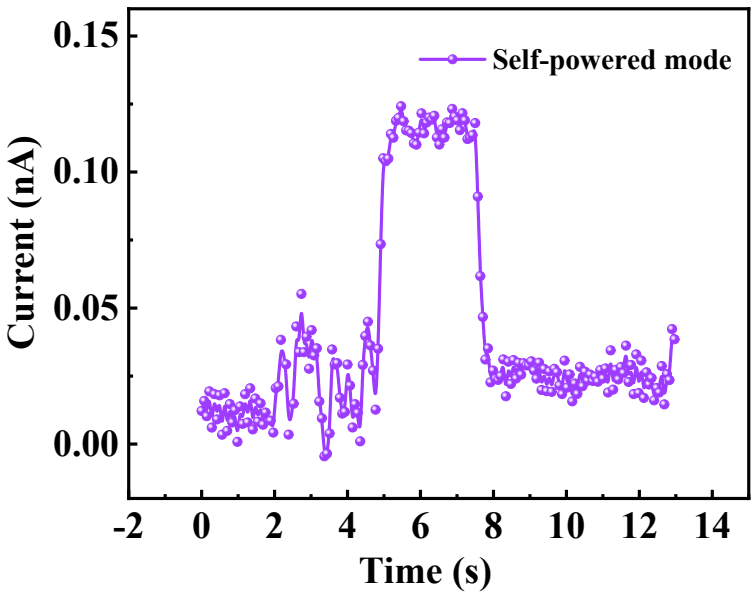


**Figure S10.** Photo response of h-BN/$MoS_2$/CuO heterostructure under illumination with wavelength of 525nm at zero bias voltage, where the device is operated in self-powered mode.

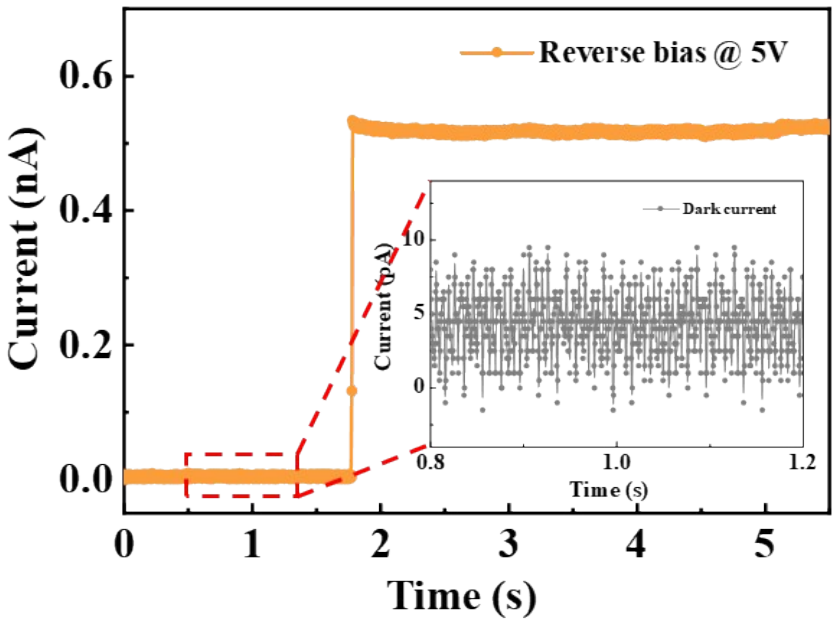


**Figure S11.** Dark current of the fs laser treated h-BN/$MoS_2$/CuO heterojunction at reverse bias @ 5V, indicating that the maximum dark current is less than 10pA.

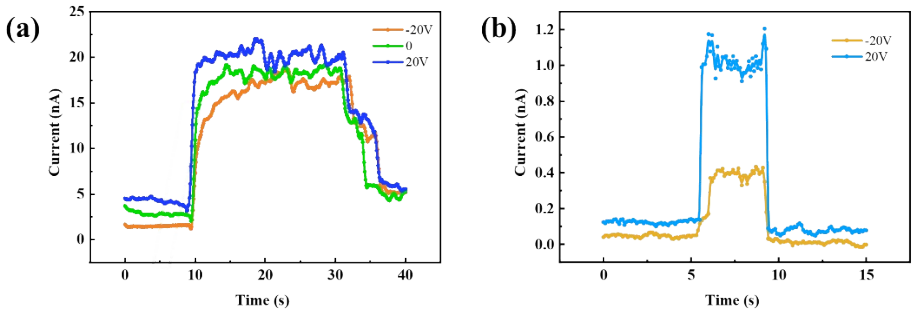


**Figure S12.** Dual functional mode of CuO-$MoS_2$ 1D-2D p-n junction under different gate voltage. (a) Time-resolved photoresponse of the heterojunction at forward bias, recorded for different values of gate voltage. (b) Time-resolved photoresponse of the device at reverse bias.

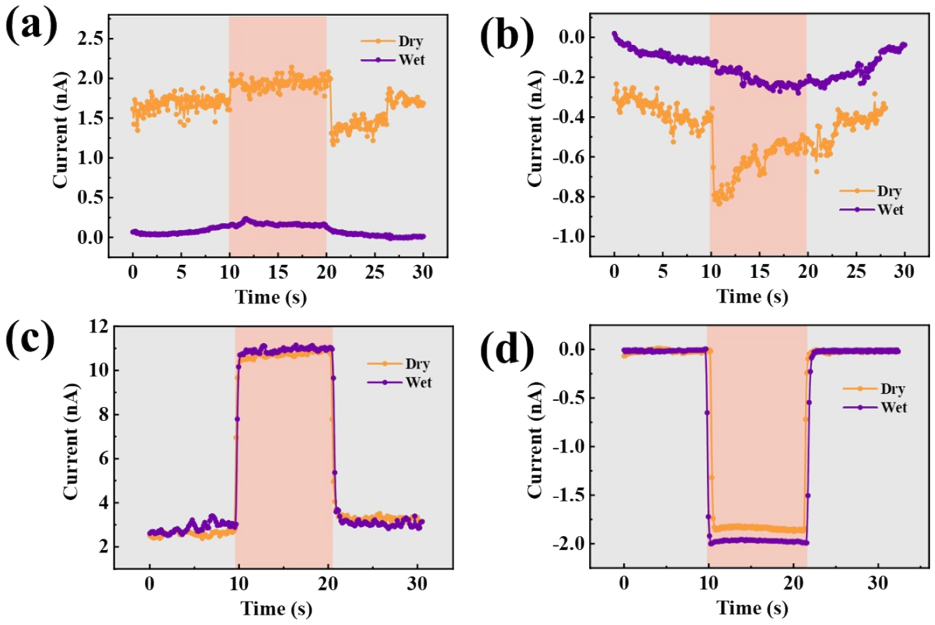


**Figure S13.** Encapsulation effect on photoresponsivity and response speed of CuO/$MoS_2$ 1D-2D devices under the humidity condition. (a) and (b) Humidity test of $MoS_2$/CuO heterostructure at forward bias and reverse bias, respectively. (c) and (d) Humidity test of h-BN/$MoS_2$/CuO heterostructure at forward bias and reverse bias, respectively.

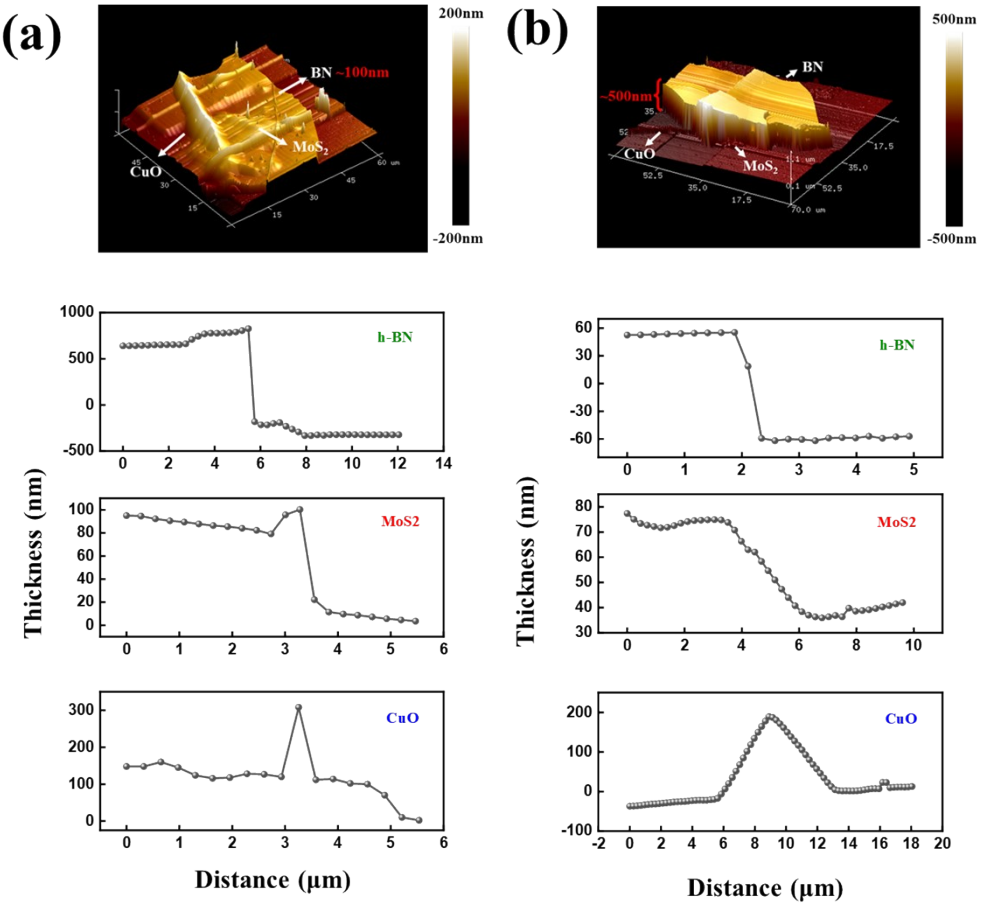


**Figure S14.** AFM images of CuO/$MoS_2$ 2D-1D van der Waals heterostructures encapsulated by (a) bulk h-BN (>500 nm) and (b) multilayer h-BN (~100 nm), respectively.

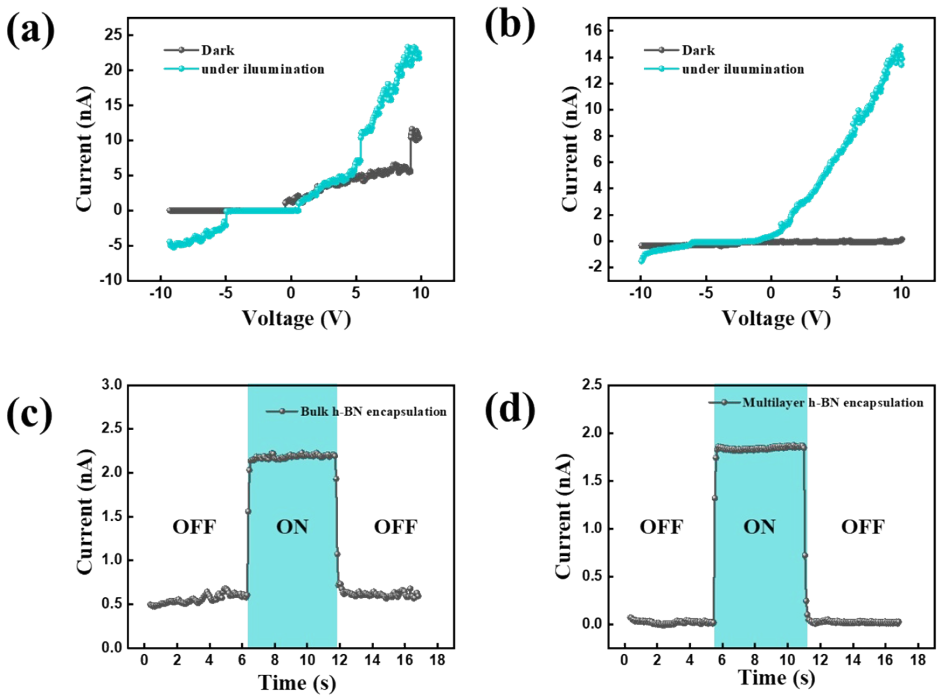


**Figure S15.** Photo response characterization of $CuO/MoS_2$ 2D-1D van der Waals heterostructures encapsulated by (a) bulk h-BN (>500 nm) and (b) multilayer h-BN (~100 nm), respectively. Photoswitching performance in wet environments (humidity ≥ 60%) of $CuO/MoS_2$ 2D-1D van der Waals heterostructures encapsulated by (c) bulk h-BN (>500 nm) and (d) multilayer h-BN (~100 nm), respectively.

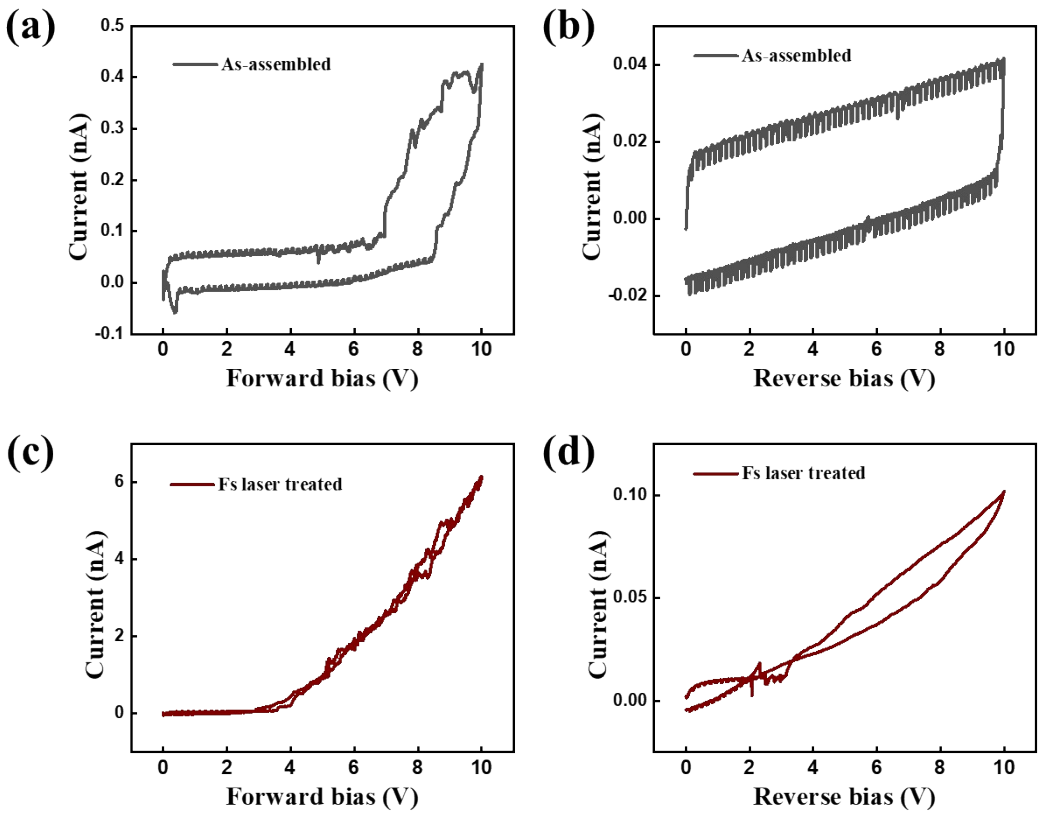


**Figure S16.** (a) and (b) I-V curve of pristine h-BN/$MoS_2$/CuO heterostructure at forward and reverse bias, which shows a significantly hysteresis. (c) and (d) I-V curve of fs laser treated h-BN/$MoS_2$/CuO heterostructure at forward and reverse bias, indicating that the fs laser irradiation is effective in minimizing the hysteresis.

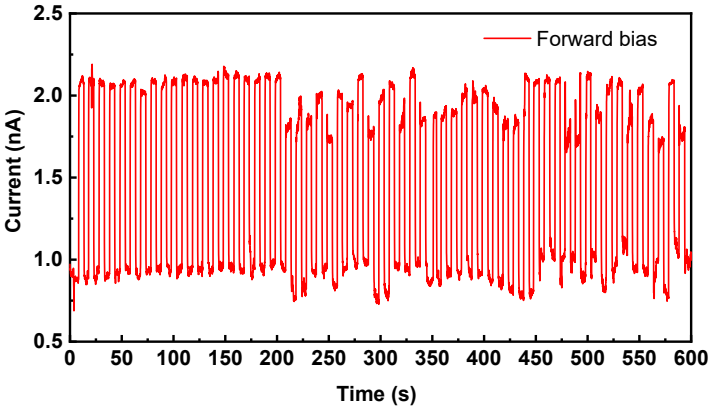


**Figure S17.** Photoswitching behavior for the heterojunction at forward bias after being left in air for 180 days.

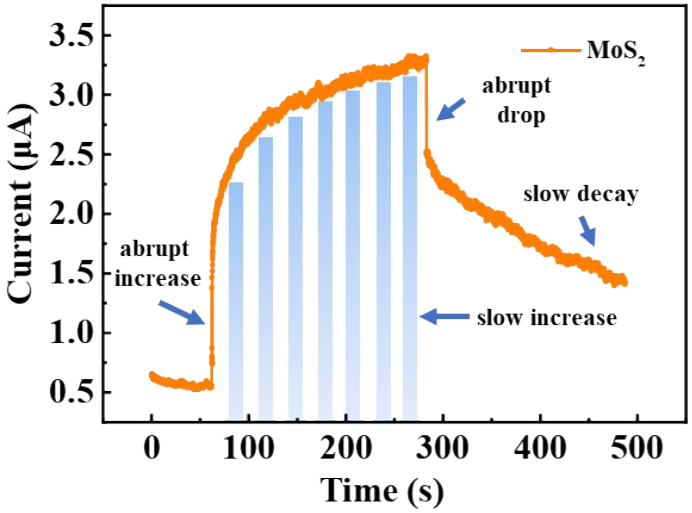


**Figure S18.** Dynamic photo response of Au-$MoS_2$-Au photodetector in a dark–light–dark cycle, indicating a significant increase of current with the measurement time caused by the increase of channel conductivity.

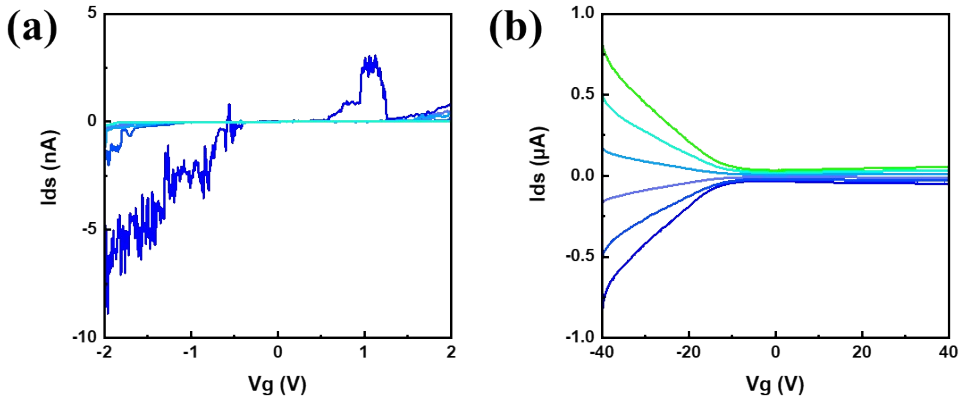


**Figure S19.** (a) $I_{ds}$-$V_g$ curve of pristine BP FET at different bias, which shows an unstable electrical performance due to the oxidation. (b) $I_{ds}$-$V_g$ curve of fs laser post-treated h-BN encapsulated BP FET at different bias, indicating that the fs laser irradiation under h-BN encapsulation will not damage the intrinsic properties of the environment-sensitive 2D material.

## Supplementary Tables

**Table R1.** Comparison of electrical and optical performances of $MoS_2$-based and mix-dimensional photodetectors. τ1: response time; τ2: decay time; HJs: Heterojunctions; MSM; metal-

semiconductor-metal

| Type | Technology | Photo responsivity | Response Speed | Dark current | Ref. |
|---|---|---|---|---|---|
| **h-BN/$MoS_2$/CuO heterostructures** | **photodiode& phototransistor** | **2500 A/W** | **$\tau_r$:2.5 ms $\tau_d$:3.5 ms** | **<10 pA** | **This work** |
| Multilayer $MoS_2$ | MSM phototransistor | 0.57 A/W | $\tau_r$:70 ms $\tau_d$:110 ms | ~500nA | [16] |
| $MoS_2$ HJs by thickness modulation | PN photodiode | 100-600 mA/W | - | ~5 pA | [17] |
| $MoS_2$/carbon quantum dot | photoconductor | 18 mA/W | 0.57s | ~500nA | [18] |
| $MoS_2$/$MoTe_2$ heterostructures | photodiode | 46 mA/W | 0.06 ms | 3 pA | [19] |
| 1D CuO/ 2D $MoS_2$ heterostructures | photodiode | ~157.6 A/W | $\tau_r$:34.6 ms $\tau_d$:51.9 ms | ~38 fA | [20] |
| 1D CdS/ 2D $WSe_2$ heterostructures | photodiode | 33.4 A/W | less than 1 s | 1.75 nA | [21] |
| 1D Te/ 2D $MoS_2$ heterostructures | photodiode | 30.1 mA/W | $\tau_r$:33.1 ms $\tau_d$:22.7 ms | 30 pA | [22] |
| 1D $Sb_2Se_3$/2D $WS_2$ heterostructures | photodiode | 1.51 A/W | less than 8 ms | - | [23] |
| 1D ZnO/ 2D $WSe_2$ heterostructures | photodiode | 0.67 A/W | less than 50 ms | 5 pA | [24] |
| 1D Se/2D InSe heterostructures | photodiode | 32 mA/W | $\tau_r$:30 ms $\tau_d$:37 ms | - | [25] |
| 1D CdS/2D $MoTe_2$ heterostructures | photodiode | 0.06 A/W | $\tau_r$:50 ms $\tau_d$:50 ms | - | [26] |
| 1D SbSI/2D $PbI_2$ heterostructures | photodiode | 15 mA/W | $\tau_r$:12 ms $\tau_d$:8 ms | 10 pA | [27] |
| 1D CsPbBr3/ 2D Bi2O2Se | photodiode | 145 A/W | $\tau_r$:0.96 ms $\tau_d$:1.36 ms | - | [28] |

# Reference


1 T. Sun, J. Huo, Y. Xiao, L. Liu, B. Feng, X. Zhai, W. Wang, G. Zou, Appl Surf Sci 2022, 575, 151709.

2 J. Chen, J. Ng, Z. Lin, C. T. Chan, Nat Photonics 2011, 5, 531.

3 H. Wan, C. Gui, D. Chen, J. Miao, Q. Zhao, S. Luan, S. Zhou, Appl. Opt. 2020, 59, 2186.

4 P. A. Williams, J. A. Hadler, R. Lee, F. C. Maring, J. H. Lehman, Opt. Lett. 2013, 38, 4248.

5 N. S. Taghavi, P. Gant, P. Huang, I. Niehues, R. Schmidt, S. Michaelis de Vasconcellos, R. Bratschitsch, M. García-Hernández, R. Frisenda, A. Castellanos-Gomez, Nano Res 2019, 12, 1691.

6 E. Garcés, O. Salas, L. F. Magaña, 2021, 8.

7 C. Song, H. Yang, F. Liu, G. J. Cheng, Nat Commun 2021, 12, 4879.

8 M. M. Furchi, D. K. Polyushkin, A. Pospischil, T. Mueller, Nano Lett 2014, 14, 6165.

9 W. Wang, X. Zeng, J. H. Warner, Z. Guo, Y. Hu, Y. Zeng, J. Lu, W. Jin, S. Wang, J. Lu, Y. Zeng, Y. Xiao, ACS Appl Mater Interfaces 2020, 12, 33325.

10 J. Seo, J. H. Lee, J. Pak, K. Cho, J.-K. Kim, J. Kim, J. Jang, H. Ahn, S. C. Lim, S. Chung, K. Kang, T. Lee, 2021, 8, 2102437.

11 S. Lukman, L. Ding, L. Xu, Y. Tao, A. C. Riis-Jensen, G. Zhang, Q. Y. S. Wu, M. Yang, S. Luo, C. Hsu, L. Yao, G. Liang, H. Lin, Y.-W. Zhang, K. S. Thygesen, Q. J. Wang, Y. Feng, J. Teng, Nat Nanotechnol 2020, 15, 675.

12 D. Shen, H. Yang, C. Spudat, T. Patel, S. Zhong, F. Chen, J. Yan, X. Luo, M. Cheng, G. Sciaini, Y. Sun, D. A. Rhodes, T. Timusk, Y. N. Zhou, N. Y. Kim, A. W. Tsen, Nano Lett 2022, 22, 3425.

13 Z. Liu, H. Qiu, C. Wang, Z. Chen, B. Zyska, A. Narita, A. Ciesielski, S. Hecht, L. Chi, K. Müllen, P. Samorì, Adv Mater 2020, 32, 2001268.

14 S. Berweger, H. Zhang, P. K. Sahoo, B. M. Kupp, J. L. Blackburn, E. M. Miller, T. M. Wallis, D. V. Voronine, P. Kabos, S. U. Nanayakkara, ACS Nano 2020, 14, 14080.

15 A. Di Bartolomeo, L. Genovese, T. Foller, F. Giubileo, G. Luongo, L. Croin, S.-J. Liang, L. K. Ang, M. Schleberger, Nanotechnology 2017, 28, 214002.

16 D.-S. Tsai, K.-K. Liu, D.-H. Lien, M.-L. Tsai, C.-F. Kang, C.-A. Lin, L.-J. Li, J.-H. He, ACS Nano 2013, 7, 3905.

17 M. Tosun, D. Fu, S. B. Desai, C. Ko, J. Seuk Kang, D.-H. Lien, M. Najmzadeh, S. Tongay, J. Wu, A. Javey, Sci. Rep. 2015, 5, 10990.

18 P. Sahatiya, S. S. Jones, S. Badhulika, Appl Mater Today 2018, 10, 106.

19 Y. Chen, X. Wang, G. Wu, Z. Wang, H. Fang, T. Lin, S. Sun, H. Shen, W. Hu, J. Wang, J. Sun, X. Meng, J. Chu, Small 2018, 14, 1703293.

20 D.-S. Um, Y. Lee, S. Lim, S. Park, H. Lee, H. Ko, ACS Appl Mater Interfaces 2016, 8, 33955.

21 P. Lin, L. Zhu, D. Li, L. Xu, Z. L. Wang, Nanoscale 2018, 10, 14472.

22 D. Zhao, Y. Chen, W. Jiang, X. Wang, J. Liu, X. Huang, S. Han, T. Lin, H. Shen, X. Wang, W. Hu, X. Meng, J. Chu, J. Wang, Adv Electron Mater 2021, 7, 2001066.

23 G. Sun, B. Li, J. Li, Z. Zhang, H. Ma, P. Chen, B. Zhao, R. Wu, W. Dang, X. Yang, X. Tang, C. Dai, Z. Huang, Y. Liu, X. Duan, X. Duan, Nano Res 2019, 12, 1139.

24 Y. T. Lee, P. J. Jeon, J. H. Han, J. Ahn, H. S. Lee, J. Y. Lim, W. K. Choi, J. D. Song, M.-C.

Park, S. Im, D. K. Hwang, 2017, 27, 1703822.

25 H. Shang, H. Chen, M. Dai, Y. Hu, F. Gao, H. Yang, B. Xu, S. Zhang, B. Tan, X. Zhang, P. Hu, Nanoscale Horiz 2020, 5, 564.

26 M.-Y. Lu, Y.-T. Chang, H.-J. Chen, Small 2018, 14, 1802302.

27 L. Sun, C. Wang, L. Xu, J. Wang, X. Liu, X. Chen, G.-C. Yi, CrystEngComm 2019, 21, 3779.

28 C. Fan, B. Dai, H. Liang, X. Xu, Z. Qi, H. Jiang, H. Duan, Q. Zhang, Adv Funct Mater 2021, 31, 2010263.